Electronic Supplementary Material (ESI) for CrystEngComm.
This journal is © The Royal Society of Chemistry 2024

Supporting Information

Two multifunctional Dy(III)-based metal-organic frameworks exhibiting proton conduction, magnetic properties and second-harmonic generation

Ya-Qing Liao, Tian-Zheng Xiong, Kang-Le Xie, Huan Zhang, Jun-Jie Hu* and He-Rui Wen

Table S1. X-ray diffraction crystallographic data for **1** and **2**.

Table S2. Selected bond lengths (Å) and bond angles (°) for **1**.

Table S3. Selected bond lengths (Å) and bond angles (°) for **2**.

Table S4. Summary of SHAPE analysis of Dy1 and Dy2 for **1**.

Table S5. Summary of SHAPE analysis of Dy1 for **2**.

Scheme 1. Synthesis of the H_4TPTC-2OMe linker.

Figure S1. IR spectra for **1** and **2**.

Figure S2 The triangular dodecahedron (TDD-8) coordination geometry Dy^{III} in **1**.

Figure S3 The Muffin coordination geometry of Dy^{III} in **2**.

Figure S4 The 2D layer of MOF **2** from different directions.

Figure S5 The simulated and experimental PXRD patterns of as-synthesized sample of **1** (a) and **2** (b).

Figure S6 TGA of **1** from 30 °C to 1000 °C.

Figure S7 TGA of **2** from 30 °C to 1000 °C.

Figure S8. Plot of proton conductivity *vs*. RH at 25 °C for **1** (a) and **2** (b).

Table S6. Nyquist plots for **1** and **2** at different humid (RH%) under 25 °C.

Table S7. The proton conductivity of **1** and **2** under variable temperature at 98% RH.

Figure S9. PXRD of compound 1 and 2 after proton conduction.

Figure S10. Temperature dependence of the magnetic susceptibility between 2 and 300 K and χ_M^{-1} *vs T* plots of MOFs **1** (a) and **2** (b). Red lines for the Curie−Weiss fitting.

Figure S11. Experimental *M* versus HT^{-1} plots of **1** (a) and **2** (b) at 2 K.

Figure S12. The in-phase(χ') and out-of-phase (χ'') components of ac magnetic susceptibility for **1** at H_{dc} = 0 Oe.

Figure S13. The in-phase(χ') and out-of-phase (χ'') components of ac magnetic susceptibility for **2** at H_{dc} = 0 Oe.

Table S8. The fitting parameters α and τ values for **1** and **2** by using CC-FIT software from 2 to 3.5 K at H_{dc} = 2 kOe.

Figure 14. Temperature dependence of the in-phase (χ') (a) and out-of-phase (χ'') (b) ac susceptibility for **2** under 2 kOe applied dc field.

Figure 15. $\ln(\chi''/\chi')$ *vs.* T^{-1} of MOF **2** under different frequency.

Materials and General Methods.

$Dy(NO_3)_3 \cdot 6H_2O$, dimethylformamide (DMF) and lactic acid adopted were commercially available without additional purification. The H_4TPTC-2OMe ligand employed was synthesized by the previous literature.[1] Elements analyses of C, H and O were performed on an Elementar Vario EL III microanalyzer. Powder X-ray diffraction (PXRD) patterns were carried out on a Rigaku D/Max-2500 diffractometer with a Cu-target tube. and the simulated PXRD patterns were acquired from the Mercury Version 1.4 software (http://www.ccdc.cam.ac.uk/products/mercury). Fourier transform infrared (FTIR) spectra were recorded on an ALPHA (Bruker) spectrophotometer with KBr pellets (400–4000 cm^{-1}). Thermogravimetric analyses (TGA) were conducted with a NETZSCH STA2500 (TG/DTA) thermal analyzer under a N_2 gas flow. The temperature varied from room temperature to 1000 °C at a heating rate of 10 °C/min. Proton conductivity measurements were tested *via* a quasi-four-electrode AC impedance technique utilizing a Solartron 1260 impedance/gain-phase analyzer. The SHG efficiency measurements were carried out on Mini NOTS 1064VT nonlinear optical test system based on powder crystalline samples adopting a modified Kurtz Perry method. Magnetic susceptibilities were obtained using a Quantum Design PPMS model 6000 magnetometer.

Proton Conductivity Measurements.

The AC impedance measurements were carried out on a Solartron 1260 impedance/gain-phase analyzer based on a quasi-four-electrode AC impedance technique. The powders of **1** and **2** were pressed into pieces under 0.1 GPa pressure and measured to be 0.63 mm for **1**, 0.86 mm for **2** in thickness and 2.5 mm in diameter by vernier calipers. Both sides of the sample are connected with gold wires through the gold paste. The proton conductivities were obtained by changing the humidity (60–98%) and the temperature (25–50 °C) over a frequency domain of 1–10^7 Hz. The proton conductivities were obtained by fitting the Nyquist plots using ZView2 software. The proton conductivities were obtained according to the formula: σ = L/(RS) (σ = proton conductivity (S cm^{-1}), L = thickness (cm) of the circular pellet, S = flat surface area (cm^2) of the circular pellets and R = bulk resistance (Ω)). The activation energy (E_a) was calculated according to the formula: $\sigma T = A \exp(E_a/k_B T)$, where σ, T, A, E_a, and k_B represent the proton conductivity (S cm^{-1}), absolute temperature (K), Boltzmann constant (eV/K), activation energy(eV), pre-exponential factor, respectively.

Table S1. X-ray diffraction crystallographic data for **1** and **2**.

	1	**2**
Formula	$C_{288}H_{248}Dy_{16}O_{160}$	$C_{24}H_{21}DyO_{13}$
Mr	8868.85	679.92
T/K	295	297
cryst syst	Orthorhombic	Triclinic
space group	*Fdd2*	$P\bar{1}$
a/Å	28.3208(13)	10.0739(5)
b/Å	39.2416(17)	10.1946(5)
c/Å	16.2646(6)	12.6937(6)
α/deg	90	76.507(1)
β/deg	90	86.196(2)
γ/deg	90	71.856(1)
V/Å^3	18075.7(13)	1204.59 (10)
Z	2	2
D_{calcd}/g cm^{-3}	1.629	1.875
μ/mm^{-1}	3.338	3.17
F(000)	8624.0	670.457
Crystal size/mm^3	0.23 × 0.23× 0.21	0.20 × 0.20 × 0.23
Reflns collected	68161	17781
GOF(F^2)	1.058	1.05
R_1[a]/wR_2[b][I >2σ(I)]	0.0256, 0.0665	0.0595, 0.0661
R_1[a]/wR_2[b] [all data]	0.0288, 0.0684	0.0409, 0.0646

[a]$R_1 = \sum||F_o|-|F_c||/\sum|F_o|$, [b]w$R_2 = [\sum w(F_o^2-Fc^2)^2/\sum w(F_o^2)^2]^{1/2}$

Table S2. Selected bond lengths (Å) and bond angles (°) for **1**.

Dy1—O17^{i}	2.301 (4)	Dy2—O11	2.286 (5)
Dy1—O6	2.312 (5)	Dy2—O15	2.288 (5)
Dy1—O12^{i}	2.330 (5)	Dy2—O5^{iii}	2.325 (5)
Dy1—O16^{ii}	2.417 (5)	Dy2—O18^{v}	2.3376 (5)
Dy1—O7	2.420 (7)	Dy2—O13	2.436 (7)
Dy1—O8	2.449 (6)	Dy2—O14	2.487 (6)
Dy1—O4^{iii}	2.463 (5)	Dy2—O15	2.288 (5)
Dy1—O1^{iii}	2.607 (5)	Dy2—O18^{v}	2.376 (5)
O17^{i}—Dy1—O6	108.4 (2)	O11—Dy2—O15	104.3 (2)
O17^{i}—Dy1—O12^{i}	76.38 (18)	O11—Dy2—O5^{v}	80.2 (2)
O6—Dy1—O12^{i}	81.19 (19)	O15—Dy2—O5^{v}	78.2 (2)
O17^{i}—Dy1—O16^{ii}	82.10 (17)	O11—Dy2—O18^{vi}	158.9 (2)
O6—Dy1—O16^{ii}	156.6 (2)	O15—Dy2—O18^{vi}	82.74 (18)
O12^{i}—Dy1—O16^{ii}	81.16 (19)	O5^{v}—Dy2—O18^{vi}	81.86 (19)
O17^{i}—Dy1—O7	147.7 (2)	O11—Dy2—O13	88.7 (3)
O6—Dy1—O7	85.5 (3)	O15—Dy2—O13	147.2 (3)
O12^{i}—Dy1—O7	77.2 (2)	O5^{vi}—Dy2—O13	74.4 (3)
O16^{ii}—Dy1—O7	75.7 (2)	O18^{vi}—Dy2—O13	75.8 (3)
O17^{i}—Dy1—O8	67.97 (19)	O11—Dy2—O14	75.0 (3)

Symmetry codes: (i) 3/4-*x*, 1/4+*y*, 3/4+*z*; (ii) -1/4+*x*, 3/4-*y*, 5/4+*z*; (iii) 3+*x*, +*y*, 1+*z*; (iv) 3/4-*x*, -1/4+*y*, -3/4+*z*; (v) 1-*x*, 1/2-*y*, -1/2+*z*; (vi) 6+*x*, +*y*, -1+*z*; (vii) 3/2-*x*, 1/2-*y*, +*z*.

Table S3. Selected bond lengths (Å) and bond angles (°) for **2**.

Dy1—O2^{ii}	2.454 (3)	Dy1—O6^{i}	2.324 (3)
Dy1—O3	2.337 (3)	Dy1—O7^{iii}	2.467 (3)
Dy1—O3^{i}	2.600 (3)	Dy1—O8^{iii}	2.494 (3)
Dy1—O4^{i}	2.442 (3)	Dy1—O9	2.389 (3)
Dy1—O5	2.309 (3)	O6^{i}—Dy1—O3^{i}	70.55 (10)
O3^{i}—Dy1—O2^{ii}	102.96 (11)	O6^{i}—Dy1—O4^{i}	81.92 (11)
O3—Dy1—O2^{ii}	143.84 (12)	O6^{i}—Dy1—O5	135.42 (11)
O4^{i}—Dy1—O2^{ii}	66.53 (11)	O7^{iii}—Dy1—O2^{ii}	115.82 (11)
O4^{i}—Dy1—O3	122.33 (10)	O7^{iii}—Dy1—O3	77.95 (11)
O4^{i}—Dy1—O3^{i}	51.01 (10)	O7^{iii}—Dy1—O3^{i}	141.16 (10)
O5—Dy1—O2^{ii}	71.61 (12)	O7^{iii}—Dy1—O4^{i}	144.77 (12)
O5—Dy1—O3	72.75 (12)	O7^{iii}—Dy1—O5	120.48 (12)
O5—Dy1—O3^{i}	72.77 (11)	O7^{iii}—Dy1—O6^{i}	77.60 (11)
O5—Dy1—O4^{i}	94.15 (12)	O8^{iii}—Dy1—O2^{ii}	68.64 (11)
O6^{i}—Dy1—O2^{ii}	141.14 (12)	O8^{iii}—Dy1—O3	102.95 (11)
O6^{i}—Dy1—O3	72.37 (11)	O8^{iii}—Dy1—O3^{i}	158.61 (10)
O8^{iii}—Dy1—O4^{i}	132.58 (10)	O9—Dy1—O3	141.19 (13)
O8^{iii}—Dy1—O5	85.85 (11)	O9—Dy1—O4^{i}	74.43 (12)
O8^{iii}—Dy1—O6^{i}	128.61 (10)	O9—Dy1—O5	145.11 (12)
O8^{iii}—Dy1—O7^{iii}	52.15 (10)	O9—Dy1—O6^{i}	76.55 (12)
O9—Dy1—O2^{ii}	73.62 (13)	O9—Dy1—O7^{iii}	73.11 (13)
O9—Dy1—O3^{i}	118.52 (11)	O9—Dy1—O8^{iii}	78.98 (11)

Symmetry codes: (i) -*x*+1, -*y*+1, -*z*+1; (ii) *x*-1, *y*, *z*; (iii) *x*, *y*+1, *z*; (iv) -*x*+1, -*y*+2, -*z*; (v) -*x*, -*y*+1, -*z*; (vi) *x*+1, *y*, *z*; (vii) *x*, *y*-1, *z*.

Table S4. Summary of SHAPE analysis of Dy1 and Dy2 for **1**.

Label	Shape	Symmetry	Distortion (τ)	
			Dy1	Dy2
OP-8	Octagon	D_{8h}	32.723	31.584
HPY-8	Heptagonal pyramid	C_{7v}	22.986	23.020
HBPY-8	Hexagonal bipyramid	D_{6h}	13.228	12.295
CU-8	Cube	Oh	8.394	7.651
SAPR-8	Square antiprism	D_{4d}	2.792	3.424
TDD-8	**Triangular dodecahedron**	$\boldsymbol{D_{2d}}$	**1.511**	**1.169**
JGBF-8	Johnson gyrobifastigium J26	D_{2d}	14.134	14.559
JETBPY-8	Johnson elongated triangular bipyramid J14	D_{3h}	25.221	26.753
JBTPR-8	Biaugmented trigonal prism J50	C_{2v}	3.356	3.616
BTPR-8	Biaugmented trigonal prism	C_{2v}	2.804	2.958
JSD-8	Snub diphenoid J84	D_{2d}	4.102	3.876
TT-8	Triakis tetrahedron	T_d	9.080	8.349
ETBPY-8	Elongated trigonal bipyramid	D_{3h}	21.096	22.214

Table S5. Summary of SHAPE analysis of Dy1 for **2**.

Label	Shape	Symmetry	Distortion (τ)
			Dy
EP-9	Enneagon	D_{9h}	33.125
OPY-9	Octagonal pyramid	C_{8v}	21.002
HBPY-9	Heptagonal bipyramid	D_{7h}	14.905
JTC-9	Johnson triangular cupola J3	C_{3v}	14.940
JCCU-9	Capped cube J8	C_{4v}	9.857
CCU-9	Spherical-relaxed capped cube	C_{4v}	8.691
JCSAPR-9	Capped square antiprism J10	C_{4v}	3.474
CSAPR-9	Spherical capped square antiprism	C_{4v}	2.554
JTCTPR-9	Tricapped trigonal prism J51	D_{3h}	4.209
TCTPR-9	Spherical tricapped trigonal prism	D_{3h}	3.497
JTDIC-9	Tridiminished icosahedron J63	C_{3v}	11.560
HH-9	Hula-hoop	C_{2v}	7.413
MFF-9	**Muffin**	$\boldsymbol{C_s}$	**1.902**

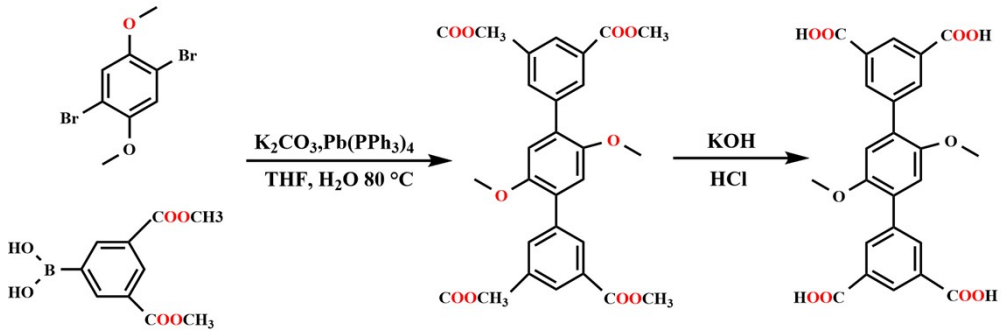

Scheme 1. Synthesis of the H_4TPTC-2OMe linker.

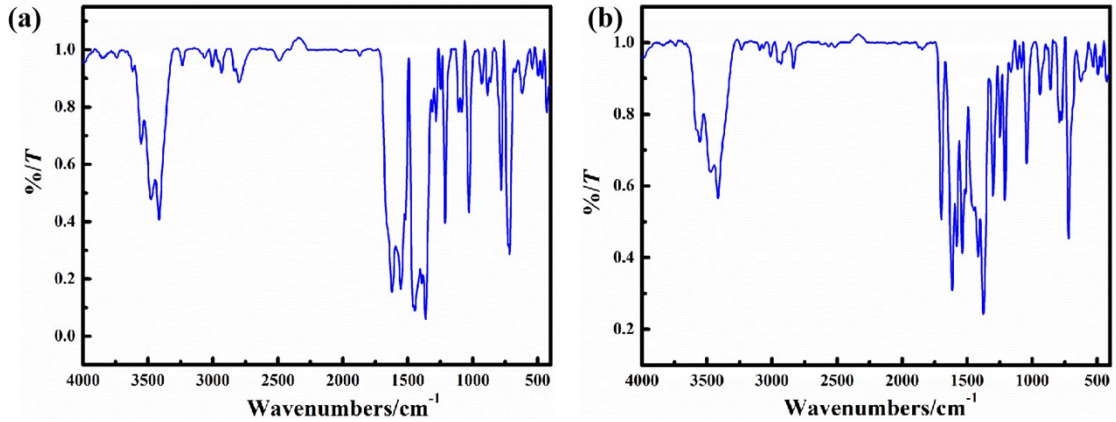

Figure S1. IR spectra for **1** and **2**.

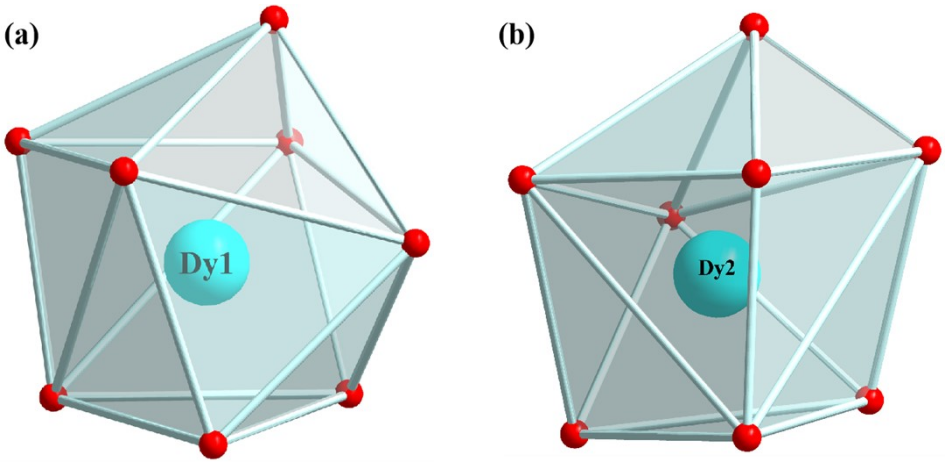

Figure S2. The triangular dodecahedron (TDD-8) coordination geometry Dy^{III} in **1**.

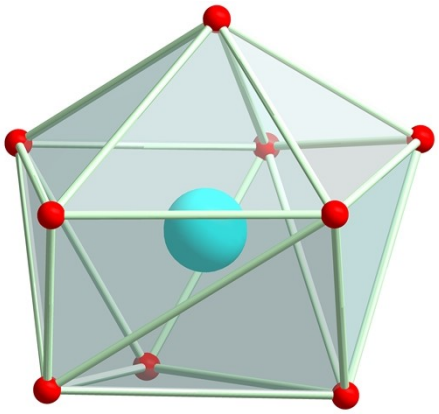

Figure S3. The Muffin coordination geometry of Dy^{III} in **2**.

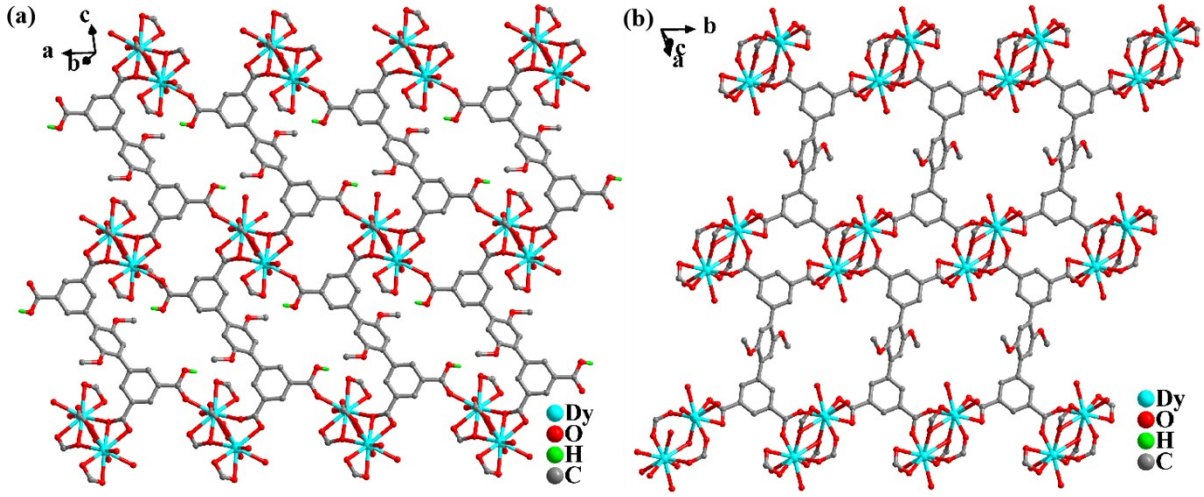

Figure S4. The 2D layer of MOF **2** from different directions.

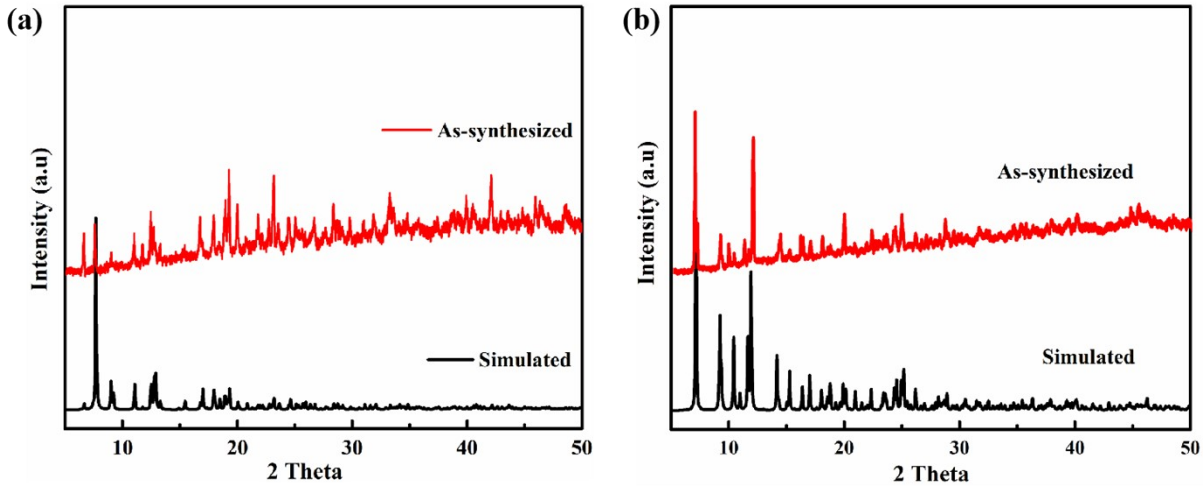

Figure S5. The simulated and experimental PXRD patterns of as-synthesized sample of **1** (a) and **2** (b).

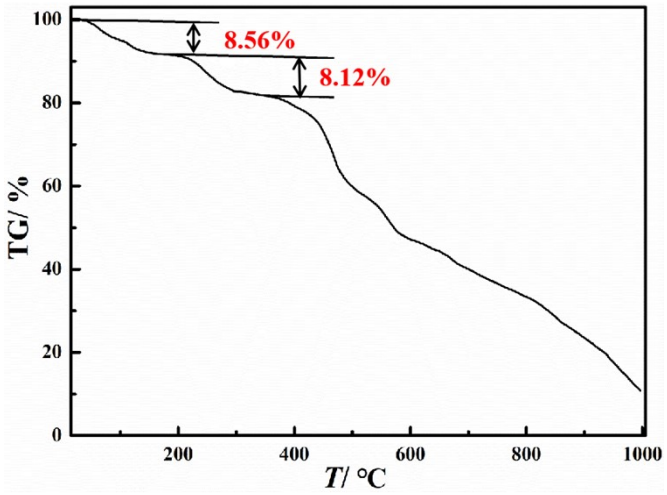

Figure S6. TGA of **1** from 30 °C to 1000 °C.

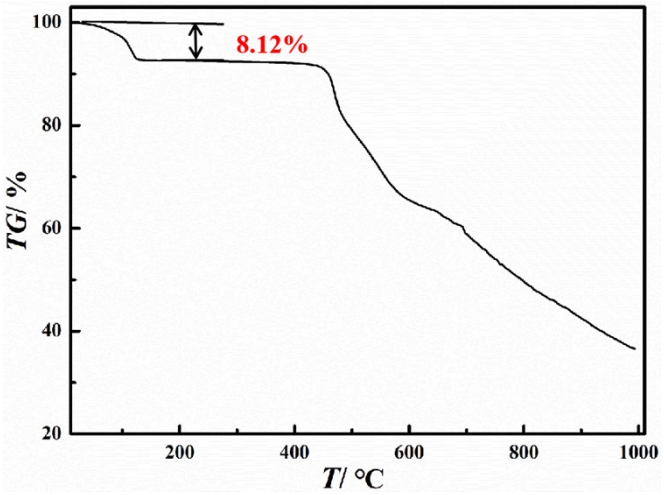

Figure S7. TGA of **2** from 30 °C to 1000 °C.

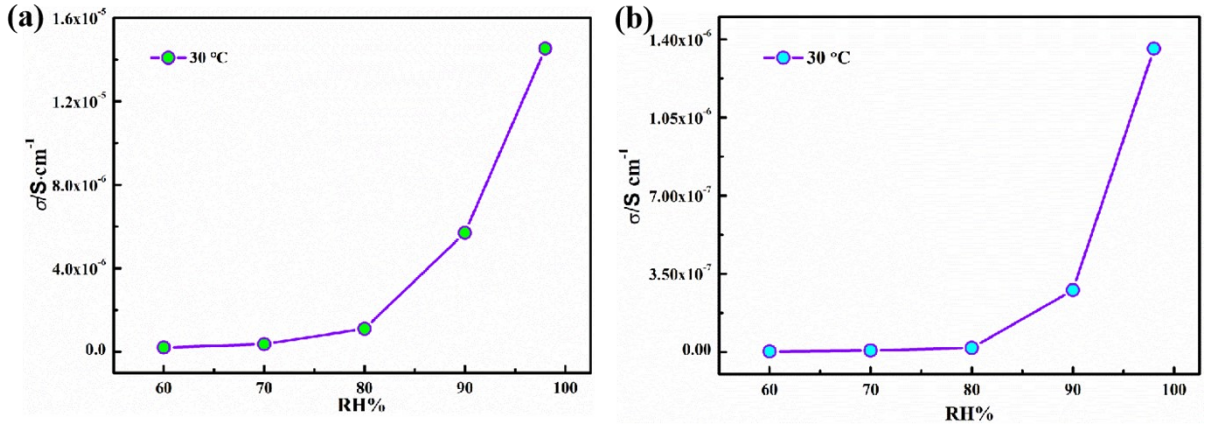

Figure S8. Plot of proton conductivity *vs*. RH at 25 °C for **1** (a) and **2** (b).

Table S6. Nyquist plots for **1** and **2** at different humid (RH%) under 25 °C.

Condition	σ (S cm^{-1})	
	RE-MOF **1**	RE-MOF **2**
60%-25 °C	2.07×10^{-7}	2.54×10^{-9}
70%-25 °C	3.72×10^{-7}	6.54×10^{-9}
80%-25 °C	1.11×10^{-6}	1.86×10^{-8}
90%-25 °C	5.70×10^{-6}	2.77×10^{-7}
98%-25 °C	1.45×10^{-5}	1.36×10^{-6}

Table S7. The proton conductivity of **1** and **2** under variable temperature at 98% RH.

Condition	σ (S cm^{-1})	
	RE-MOF **1**	RE-MOF **2**
25 ℃-98%RH	1.45×10^{-5}	1.36×10^{-6}
30 ℃-98%RH	2.57×10^{-5}	1.99×10^{-6}
35 ℃-98%RH	4.50×10^{-5}	2.65×10^{-6}
40 ℃-98%RH	6.98×10^{-5}	3.13×10^{-6}
45 ℃-98%RH	1.33×10^{-4}	3.34×10^{-6}
50 ℃-98%RH	1.69×10^{-4}	3.52×10^{-6}

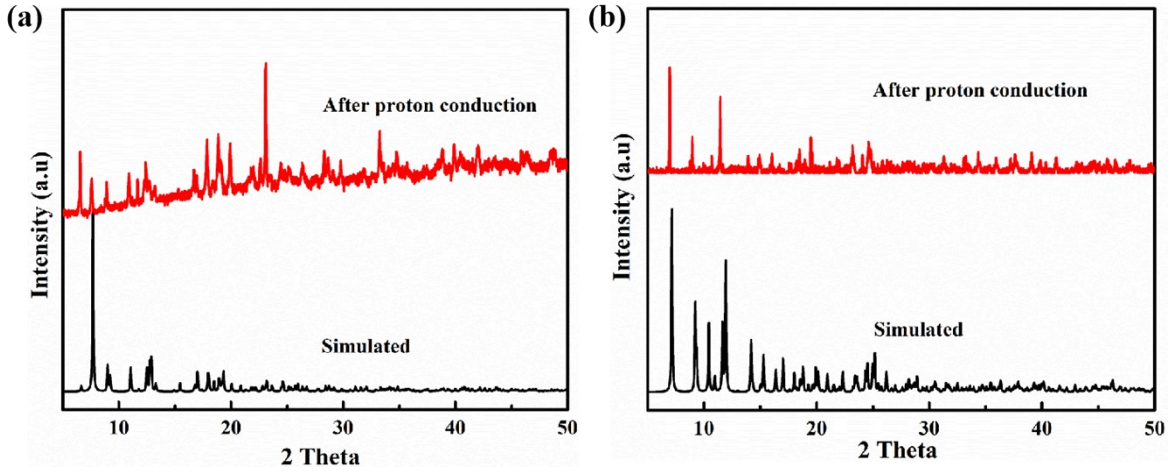

Figure S9. PXRD of compound **1** and **2** after proton conduction.

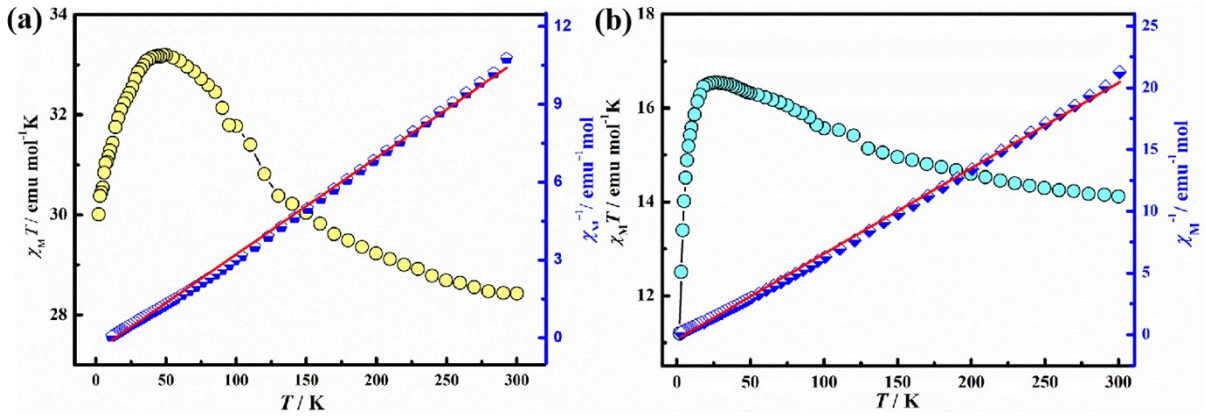

Figure S10. Temperature dependence of the magnetic susceptibility between 2 and 300 K and χ_M^{-1} *vs T* plots of MOFs **1** (a) and **2** (b). Red lines for the Curie−Weiss fitting.

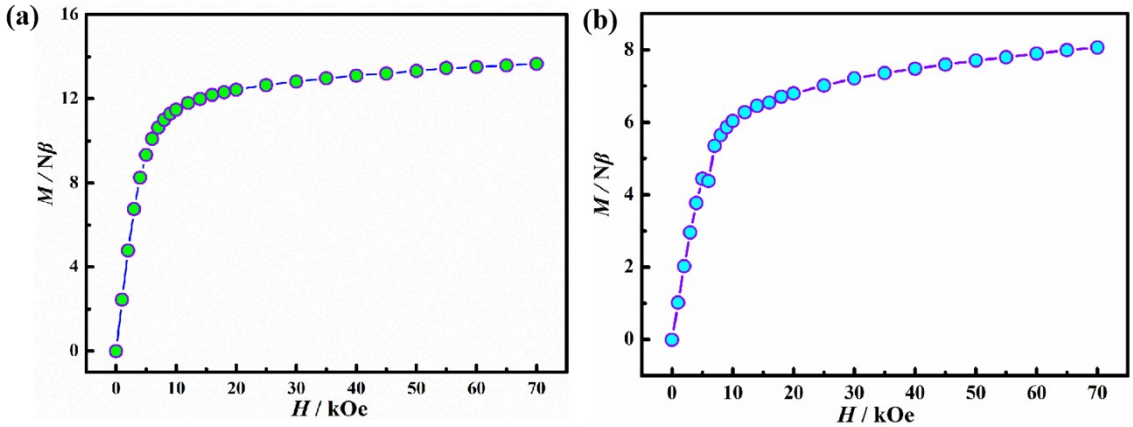

Figure S11. Experimental M versus HT^{-1} plots of **1** (a) and **2** (b) at 2 K.

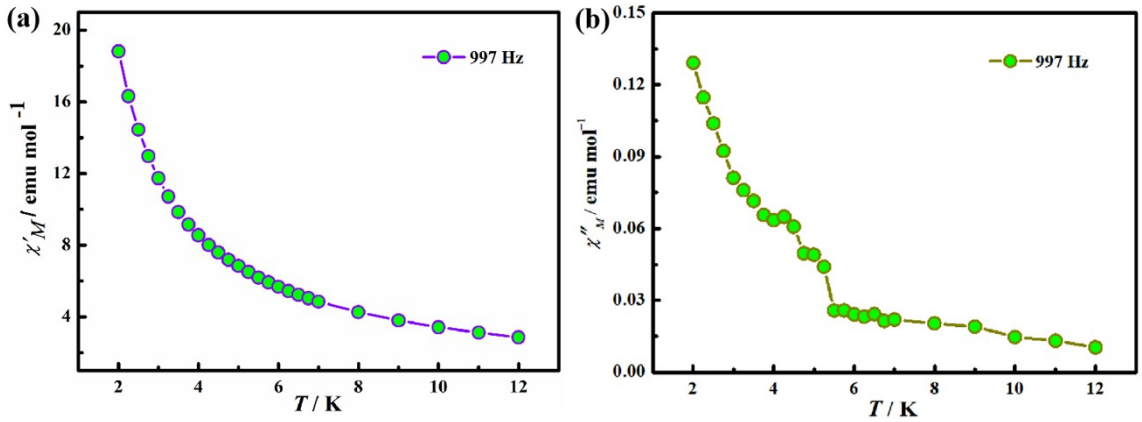

Figure S12. The in-phase(χ') and out-of-phase (χ'') components of ac magnetic susceptibility for **1** at H_{dc} = 0 Oe.

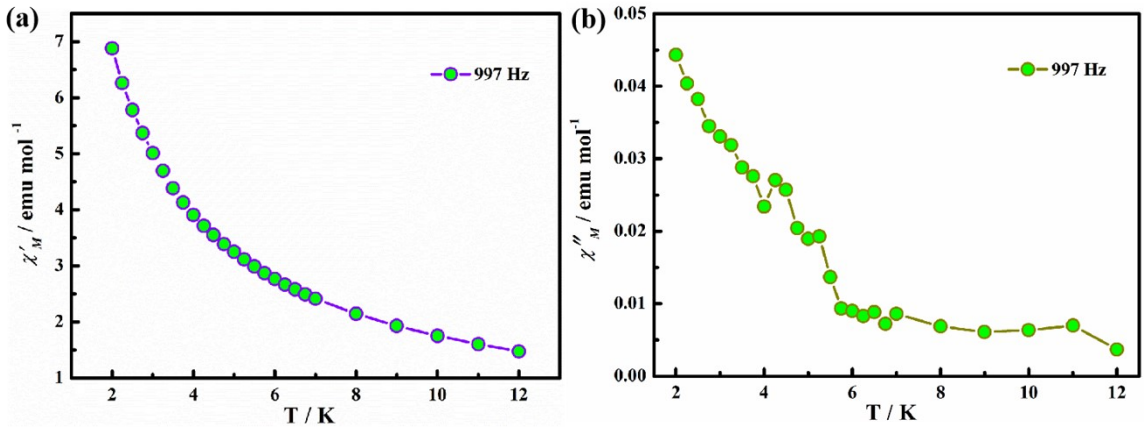

Figure S13. The in-phase(χ') and out-of-phase (χ'') components of ac magnetic susceptibility for **2** at H_{dc} = 0 Oe.

Table S8. The fitting parameters α and τ values for **1** and **2** by using CC-FIT software from 2 to 3.5 K at H_{dc} = 2 kOe.

T	α_1	τ_1 / s	α_2 / s	τ_2 / s
2.0 K	0.38	5.0×10^{-4} s	0.12	0.32 s
2.5 K	0.45	4.4×10^{-4} s	0.14	0.21 s
3.0 K	0.47	4.2×10^{-4} s	0.23	0.18 s
3.5 K	0.47	5.0×10^{-4} s	0.19	0.12 s

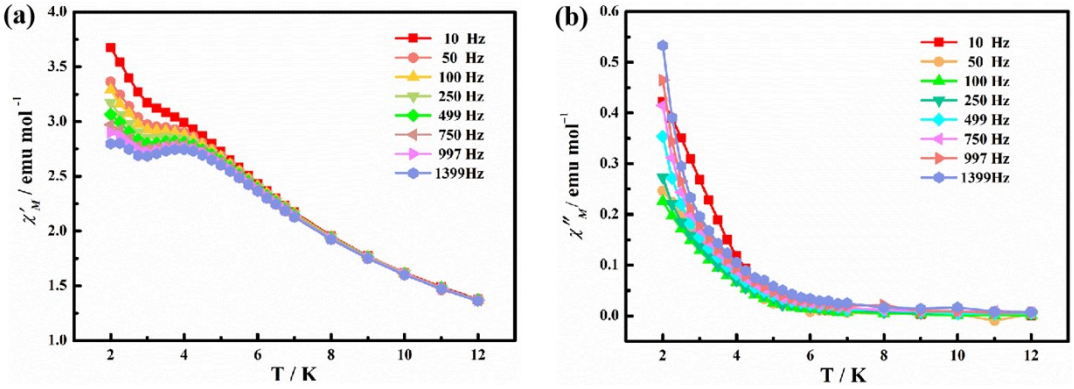

Figure S14. Temperature dependence of the in-phase (χ′) (a) and out-of-phase (χ″) (b) ac susceptibility for **2** under 2 kOe applied dc field.

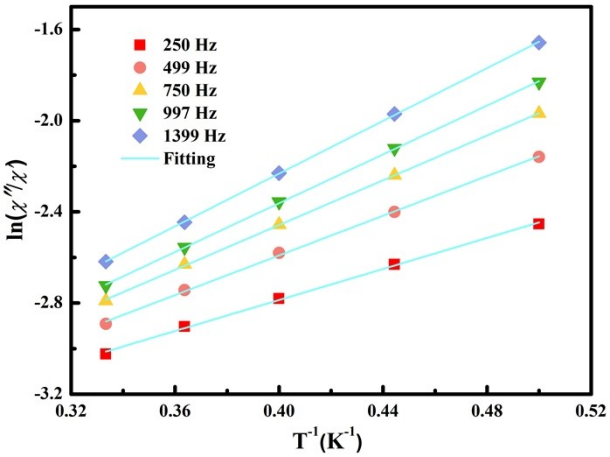

Figure S15. ln(χ″/χ′) *vs.* T^{-1} of MOF **2** under different frequency.

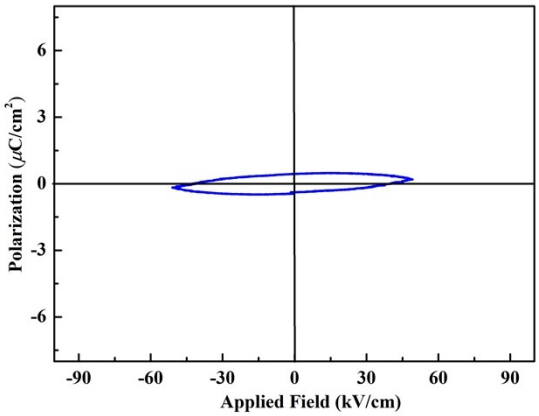

Figure S16. The measurement of ferroelectric hysteresis loops of MOF **1**.

1 J. W Liu, X. Han, Y. T. Lu, S. Wang, D. Zhao and C. X. Li, *Inorg. Chem*., 2021, **60**, 4133−4143.